Effects of Bath Gas and NO x Addition on n -Pentane Low-Temperature Oxidation in a Jet-Stirred Reactor

Lorena Marrodán, Yu Song, Marco Lubrano Lavadera, Olivier Herbinet, Mara de Joannon, Yiguang Ju, María U Alzueta, Frédérique Battin-Leclerc

Effects of Bath Gas and NOx Addition on *n*-Pentane Low-Temperature Oxidation in a Jet-Stirred Reactor

Lorena Marrodán[1], Yu Song[2], Marco Lubrano Lavadera[3], Olivier Herbinet[2], Mara de Joannon[3], Yiguang Ju[4], María U. Alzueta[1], Frédérique Battin-Leclerc[3,*]

[1] Aragón Institute of Engineering Research (I3A), Department of Chemical and Environmental Engineering, University of Zaragoza, 50009 Zaragoza, Spain
[2] Laboratoire Réactions et Génie des Procédés, CNRS-Université de Lorraine, 54000 Nancy, France
[3] Istituto di Ricerche sulla Combustione—C.N.R., 80125 Napoli, Italy
[4] Department of Mechanical and Aerospace Engineering, Princeton University, Princeton, New Jersey 08544, United States

Published in Energy & Fuels (2019), 33, 6, 5655-5663

Abstract

The oxidation of *n*-pentane (C_5H_{12}) in different bath gases (He, Ar, and CO_2) and in Ar with NO_2 or NO addition has been studied in a jet-stirred reactor at 107 kPa, temperatures between 500 and 1100 K, with a fixed residence time of 2.0 s, under stoichiometric conditions. Four different quantification diagnostics were used: gas chromatography, a chemiluminescence NO_x analyzer, continuous wave cavity ring-down spectroscopy, and Fourier transform infrared spectroscopy. The results showed that the onset temperature of the fuel reactivity was the same (575 K) regardless of the type of bath gases. Although the low-temperature fuel oxidation window was not affected by the type of bath gas, the *n*-pentane conversion was slightly larger when diluted in Ar through the negative temperature coefficient (NTC) region (625–725 K). Above 800 K, the reactivity according to the diluent was in the order CO_2 > Ar > He. In the presence of NO_2 or NO, it was found that the consumption rate of *n*-pentane exhibited a different trend below 700 K. The presence of NO_2 did not modify the fuel conversion below 675 K. On the contrary, NO addition increased the onset temperature of the fuel reactivity by 75 K and almost no NTC zone was observed. This clearly indicated that NO addition inhibited *n*-pentane oxidation below 675 K. Above 700 K, *n*-pentane conversion was promoted by the presence of both NO_x additives. The intermediate species HONO was quantified, and a search for HCN and CH_3NO_2 species was also attempted. A new detailed kinetic mechanism was developed, which allowed a good prediction of the experimental data. Reaction rate and sensitivity analyses were conducted to illustrate the different kinetic regimes induced by the NO_x addition. The inhibition by NO of the *n*-pentane oxidation below 675 K can be explained by its direct reaction with $C_5H_{11}O_2$ radicals disfavoring the classical promoting channels via isomerizations, second O_2 addition, and formation of ketohydroperoxides, the well-known branching agents during alkane oxidation. With respect to NO_2 addition, the major consumption route is via $NO_2 + CH_3 = NO + CH_3O$, which is not directly related to the direct fuel consumption. HONO formation mainly derives from NO_2 reacting with CH_iO (i = 2, 3). The reaction, HONO + M = OH + NO + M, is one of the most sensitive reactions for HONO depletion.

1. Introduction

To meet the demand of stringent regulations, current engines are usually equipped with exhaust gas recirculation (EGR), which shows significant advantage for emissions abatement [1], because it increases dilution and decreases the temperature in the combustion chamber.

When using EGR, the fuel combustion properties are altered by the presence of great amounts of carbon dioxide and water induced by the recirculation of exhausted gases. Such species may have both thermal and chemical effects on fuel oxidation [2–8]. Lubrano Lavadera et al. [9] provided a summary of the experimental and numerical studies made before 2016, which have investigated the effects of CO_2 on combustion properties. They also observed that propane oxidation was significantly altered by CO_2 addition in a jet-stirred reactor (JSR) at atmospheric pressure at temperatures between 720 and 900 K. They found that, at high temperatures, CO_2 inhibited the CO oxidation via the reactions $CO_2 + H = CO + OH$ and $H + O_2 + M = HO_2 + M$ because of the high CO_2 three-body collisional efficiency. Both reactions competed with the $H + O_2 = OH + O$ reaction, diminishing the system reactivity. Di et al. [10] studied the effects of different diluents, including Ar, N_2, and CO_2, on the low-temperature ignition processes of *iso*-octane and *n*-heptane using a rapid compression machine. The experimental and modeling results confirmed that the bath gas composition had a significant impact on ignition under conditions exhibiting two-stage ignition within the negative temperature coefficient (NTC) region. However, the authors claimed that the bath gas composition had little impact on the first-stage ignition at any of the conditions studied. For temperatures below 800 K, the major impact of the buffer gas composition was due to thermal effects. The chemical effect increased with increasing temperature. In the two aforementioned papers [9,10], the authors recommended further investigation of the effect of high concentrations of CO_2 on fuel conversion.

Besides water and CO_2, NO_x (mainly NO and NO_2) are also present in significant amounts among the exhausted gases used in EGR. They play an important role in changing the reactivity of the fresh inlet fuel and consequently altering the ignition delay times [11–15] and product emissions. [16–27]. A typical small-size component of gasoline surrogates is *n*-pentane. Many efforts were undertaken to study the oxidation of neat *n*-pentane [28–34] or its role as a dual fuel [35]. However, reports in terms of the effect of NO_x addition on *n*-pentane oxidation are still scarce.

In 1996, Prabhu et al. [36] investigated the effect of NO addition on 1-pentene oxidation in a pressurized (6 atm) flow reactor between 600 and 800 K. Fuel reactivity and major products were determined using gas chromatography (GC) and Fourier transform infrared (FTIR) spectroscopy. Although this fuel was unsaturated, an alkane-type behavior was observed for 1-pentene, with an NTC behavior, which was suppressed in the presence of NO. No kinetic model was used to reproduce the experimental data. In 2005, Glaude et al. [37] proposed a detailed kinetic model for the mutual oxidation of NO and *n*-pentane between 600 and 1000 K in an atmospheric pressure quartz flow reactor. They pointed out that the reactions of NO with HO_2 and with alkylperoxy (ROO) radicals releasing OH or RO radical were responsible for the whole system oxidation acceleration. Recently, Zhao et al. [38,39] studied the NO_x sensitization effects on *n*-pentane oxidation in an atmospheric JSR between 500 and 800 K. The fuels, both NO and NO_2, and several C_1–C_2 products were studied by electron impact molecular beam mass spectrometry, μGC, and Faraday rotation spectrometry. The authors also developed a kinetic model to explain the observed NTC retarding phenomenon in the presence of NO_x. They proposed HONO as an

important intermediate species during the oxidation process involving nitrogen-containing species.

For atmospheric chemistry purpose, several attempts were made to identify and quantify HONO [40−42]. The absorption spectrum of HONO was first measured by Jain et al. [42] with the aid of continuous wave cavity ring-down spectroscopy (cw-CRDS). The cross section of HONO, which is essential for its quantification, was determined. Regarding combustion studies, Chai and Goldsmith [43] calculated the rate coefficients for the H-abstraction reactions, H_2 + NO_2 and CH_4 + NO_2, leading to the formation of HONO. To the authors' best knowledge, during the oxidation of a fuel in the presence of NO_x, HONO was only detected with cw-CRDS at CNRS-Nancy [44,45]. In our first attempt, methane was adopted to represent a biogas surrogate fuel in the presence of NO_x. It was found that HONO signals were below the estimated/calculated detection limit (3 ppm) [44]. More recently, HONO signals were successfully identified and quantified during *n*-pentane JSR oxidation in the presence of NO [45].

In this context, following our previous work on neat *n*-pentane low-temperature oxidation performed in an atmospheric JSR using GC and quantifying a wide range of C_0–C_5 products [30], we present here a study of the effect of diluents (He, Ar, and CO_2) and of NO_x addition on *n*-pentane oxidation at temperatures ranging from 500 to 1100 K. NO_x species were studied by chemiluminescence, the amount of HONO was quantified by means of cw-CRDS, and a search for intermediate species, CH_3NO_2 and HCN, was made with the aid of FTIR. A new detailed kinetic mechanism was developed and used to interpret the experimental data. The present study under stoichiometric conditions, with different used bath gases and with a large range of analyzed species including HONO, will significantly enlarge the database already started by Zhao et al. [38,39] on the same chemical system.

2. Experimental Setup

The experimental setup used was a laboratory-scale spherical fused silica JSR (volume of 81.2 cm^3; detailed description provided elsewhere [46]). The liquid *n*-pentane was filled into a tank and pressurized with He. The flow rate of *n*-pentane was controlled by a Coriolis flow controller. After the evaporation in a heat exchanger, the gaseous *n*-pentane, along with the gas diluent and oxygen, was premixed before entering in an annular preheating zone and to the reactor afterward through four different nozzles. These nozzles created high turbulence, which results in homogeneous distributions of mixture compositions and temperature in the reactor. The residence time inside the preheating zone was only ≈1% with respect to that in the reactor, which was kept fixed at 2.0 s (±0.1 s) within all the experiments performed. Both the reactor and the preheating zone were heated using Thermocoax resistances.

The reactor temperature was measured by a type-K thermocouple (±5 K) located at the center of the reactor. The pressure in the reactor was controlled by a needle valve (±0.2 kPa) positioned downstream of the reactor and kept constant at 107 kPa (800 Torr). Argon, helium, carbon dioxide, oxygen, NO, and NO_2 were provided by Messer (purities of 99.99%). The flow rates of the gases were controlled by mass flow controllers (±0.5%).

The gases leaving the reactor were analyzed online using four analytical techniques:

- Three gas chromatographs were equipped with three columns (carbosphere-packed column, PlotQ capillary column, and an HP-5 capillary column), a thermal conductivity detector, and a flame ionization detector. The previous product identification made using GC–MS operating with electron ionization [30] was also used in the present work.

- A chemiluminescence NO_x analyzer (Thermo Scientific Model 42i) was adopted to measure the concentration of NO and NO_2. The quantitative range is 0–5000 ppm for NO and 0–500 ppm for NO_2 with 0.1 ppm sensitivity. Two pumps were used for outlet and bypass channels, respectively.

- An FTIR spectrometer (Thermo Scientific Antaris) was used to detect the CH_3NO_2 (if any) and HCN (if any) species, see more details in ref [44].

- A homemade cw-CRDS infrared spectrometer was used to detect H_2O, CH_2O, and HONO species, the description of this instrument is also provided in ref [47].

The uncertainty in the species concentration measurements using the different diagnostic instruments is estimated to be ±5%, except for the FTIR and CRDS measurements, for which it can be estimated as ±10–15%.

3. Kinetic Model

The new chemical kinetic mechanism developed in the present work includes the *n*-pentane mechanism previously developed by the Galway group and successfully used in previous *n*-pentane oxidation studies [30,31] and an updated C_0–C_1 NO_x submechanism from the Princeton group [38]. This last submechanism already contains reactions of C_5 alkoxy radicals with NO to produce aldehydes and HNO. Additional reactions to merge/join the *n*-pentane mechanism and the NOx submechanism are included in our new mechanism. The added reactions shown in Table 1 are written by analogy with the work of Glaude et al. [37] for *n*-pentane/*n*-butane oxidation in the presence of NO and that of Anderlohr et al. [48] for the oxidation of engine surrogate fuels (*n*-heptane, *iso*-octane, and toluene) in the presence of NO.

The added reactions include the reactions of C_2–C_5 alkyl radicals with NO_2 to give NO and the corresponding alkoxy radicals. The kinetic parameters for those reactions were taken similar to those proposed by Glarborg et al. [49] for the reaction $CH_3 + NO_2 = CH_3O + NO$ (with an uncertainty around a factor of 2).

The C_2–C_5 peroxy radicals can react with NO to also produce the corresponding alkoxy radicals; in the case of hydroperoxy peroxypentyl radicals, the decomposition of the alkoxy radicals in formaldehyde, propene, and hydroxyl radical is directly written. The abstractions by NO_2 of H-atoms from *n*-pentane and of the aldehydic H-atom from C_2–C_5 aldehydes leading to HONO are also considered. Alkyl radicals can react with HNO to give NO and the corresponding alkanes. Finally, the combinations between alkyl radicals and NO_2 are also written.

Table 1. Reactions Included To Join Both Galway and Princeton Mechanisms[a]

Reaction	A	n	E_a	Source
$R\cdot+NO_2=RO\cdot+NO$[a]	4.00×10^{13}	-0.2	0	48
$C_2H_5\cdot+NO_2=NO+C_2H_5O\cdot$	4.00×10^{13}	-0.2	0	49
$C_3H_7\cdot+NO_2=NO+C_3H_7O\cdot$[b]	4.00×10^{13}	-0.2	0	49
$C_4H_9\cdot+NO_2=NO+C_4H_9O\cdot$[b]	4.00×10^{13}	-0.2	0	49
$RO_2\cdot+NO=RO\cdot+NO_2$[a]	2.53×10^{12}	0.0	-358	50
$C_2H_5O_2\cdot+NO=C_2H_5O\cdot+NO_2$	2.53×10^{12}	0.0	-358	50
$C_3H_7O_2\cdot+NO=C_3H_7O\cdot+NO_2$[b]	2.53×10^{12}	0.0	-358	50
$C_4H_9O_2\cdot+NO=C_4H_9O\cdot+NO_2$[b]	2.53×10^{12}	0.0	-358	50
$\cdot OOQOOH+NO=2CH_2O+C_3H_6+NO_2+OH$[a]	4.70×10^{12}	0.0	-358	48
$CH_3CHO+NO_2=CH_3\cdot+CO+HONO$	8.35×10^{-11}	6.68	8300	48
$C_2H_5CHO+NO_2=C_2H_5\cdot+CO+HONO$	8.35×10^{-11}	6.68	8300	48
$C_3H_7CHO+NO_2=C_3H_7\cdot+CO+HONO$[b]	8.35×10^{-11}	6.68	8300	48
$C_4H_9CHO+NO_2=C_4H_9\cdot+CO+HONO$[b]	8.35×10^{-11}	6.68	8300	48
$HNO+NO_2=HNO_2+NO$	3.00×10^{11}	0.0	1988	51
$Y\cdot+NO_2=$acrolein$+R'\cdot+NO$[c]	2.35×10^{13}	0.0	0.0	52
$RH+NO_2=R\cdot+HONO$[a,d]	(α) 2.2×10^{13}	0.0	31100	53
	(β) 5.8×10^{12}	0.0	28100	
$R\cdot+HNO=NO+RH$[a,e]	1.47×10^{11}	0.76	349	54
$C_2H_5\cdot+HNO=NO+C_2H_6$[e]	1.47×10^{11}	0.76	349	54
$C_3H_7\cdot+HNO=NO+C_3H_8$[b,e]	1.47×10^{11}	0.76	349	54
$C_4H_9\cdot+HNO=NO+C_4H_{10}$[b,e]	1.47×10^{11}	0.76	349	54
$RNO_2(+M)=R\cdot+NO_2(+M)$[a] (high pressure)	1.80×10^{17}	0.0	58500	48
Fall off Parameter Fc =0.183 (low pressure)	1.3×10^{18}	0.0	42000	
$C_2H_5NO_2(+M)=C_2H_5\cdot+NO_2(+M)$ (high pressure)	1.80×10^{17}	0.0	58500	48
Fall off Parameter Fc =0.183 (low pressure)	1.3×10^{18}	0.0	42000	
$C_3H_7NO_2(+M)=C_3H_7\cdot+NO_2(+M)$[b] (high pressure)	1.80×10^{17}	0.0	58500	48
Fall off Parameter Fc =0.183 (low pressure)	1.3×10^{18}	0.0	42000	
$C_4H_9NO_2(+M)=C_4H_9\cdot+NO_2(+M)$[b] (high pressure)	1.80×10^{17}	0.0	58500	48
Fall off Parameter Fc =0.183 (low pressure)	1.3×10^{18}	0.0	42000	

[a] Kinetic parameters of the form $k = A \times T^n \times \exp(-E_a/RT)$. Units: A is in cm^3, mol, and s; Ea is in cal/mol.
[b] R•, RO•, ROO•, and •OOQOOH are pentyl radical isomers, and the derived alkoxy, pentylperoxy, and hydroperoxy peroxypentyl radicals, respectively.
[c] For C_3H_7• and C_4H_9•, both linear isomers are considered.
[d] Y• are the C_3–C_5 resonance-stabilized alkenyl radicals considered in the *n*-pentane model, R′• is an H-atom or a C_1–C_2 alkyl radicals.
[e] α: kinetic parameters per primary H-atom, β: kinetic parameters per secondary H-atom.
[f] The rate constant has been taken as equal to that of reaction $CH_3 + HNO = CH_4 + NO$.

Moreover, the chemistry of HONO is also updated by the adoption of the rate constant for NO + OH (+M) = HONO (+M) [55], along with a modified third-body coefficient for Ar (coefficient of 0.1). The kinetic parameters for the HONO forming reaction ($NO_2 + HO_2 = HONO + O_2$) are adopted following Rasmussen et al. [22] and those of the reaction associated with OH radical attacking HONO to form NO_2 and H_2O are implemented following Burkholder et al. [56]. Two channels are

considered for the reaction of HNO with NO_2, one giving HNO_2 and NO and the other producing HONO + NO.

The complete mechanism, which involves 832 species and includes 4218 reactions, is provided as the Supporting Information of this paper in CHEMKIN format, along with thermodynamic properties. The thermodynamic data for the involved species have been taken from the same sources as in the two original mechanisms [30,38]. The present mechanism is able to reproduce experimental data from the literature [38,39] as shown in Figures S1–S4 in the Supporting Information.

4. Results

The experiments for the neat *n*-pentane oxidation with different bath gases (He, Ar, and CO_2) and for the oxidation of *n*-pentane doped with NO and NO_2 diluted in argon were carried out under stoichiometric conditions over the 500–1100 K temperature range. Equivalence ratios were calculated neglecting the amounts of added NOx compounds, which were around 4–10% that of *n*-pentane [this is to keep the inlet fuel and oxygen mole fractions (mole fractions) constant in all experiments]. The experimental conditions investigated in this study are presented in Table 2. A spreadsheet including all the experimental data, including N-atom balance, is provided in the Supporting Information.

Table 2. Experimental Conditions (T = 500–1100 K; P = 107 kPa; Residence Time 2 s; X_i is the Mole Fraction of Species i)

Exp.	$X_{n\text{-pentane}}$	X_{NO} ppm	X_{NO2} ppm	X_{O2}	Φ	Bath gas
1	0.01	-	-	0.08	1	Ar
2	0.01	-	-	0.08	1	He
3	0.01	-	-	0.08	1	CO_2
4	0.01	1000	-	0.08	1	Ar
5	0.01	500	-	0.08	1	Ar
6	0.01	-	400	0.08	1	Ar

Numerical calculations were conducted with the CHEMKIN-PRO software package [57]. Transient solver was applied in the simulation tasks with sufficient time allowed to reach the steady-state solution.

4.1. Experimental Results and Comparison with Simulations

In this part, we present the experimental results obtained first for the different used bath gases and then with the addition of NO_x. In both cases, the experimental results are compared with predictions using the aforementioned model. In all the figures shown in this part, experimental results are denoted by symbols and simulations by lines.

4.1.1. Oxidation of Neat n-Pentane: The Effect of Different Bath Gases

Figure 1 shows the temperature dependence between 500 and 1100 K of the mole fractions of *n*-pentane and CO using the three different bath gases, Ar, He, and CO_2 (exp. 1–3 in Table 2). The temperature of the reactivity onset is approximately 575 K, regardless of the bath gas. As temperature increases to 625 K, the starting temperature of the NTC zone, the conversion of

n-pentane with Ar as the carrier gas is slightly higher than that when using He and CO_2. However, *n*-pentane is more reactive with CO_2 as the carrier gas compared to He and Ar over the temperature range between 800 and 900 K. For CO mole fraction, in the 850–1000 K temperature range, modeling predictions do not show as much influence of the carrier gas as it can be seen in the experimental results.

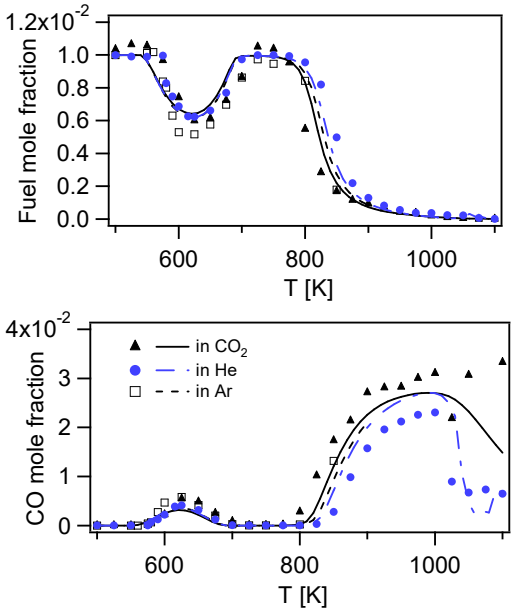

Figure 1. Temperature dependence of *n*-pentane and CO mole fraction with different bath gases. Symbols represent experiments, and lines represent simulations.

At the highest temperatures, the CO amount is the largest for the CO_2-diluted mixtures. Note that dynamic behaviors (oscillations) occur when the temperature is above 850 K with Ar as a carrier gas, which explains why the data, neither experimental nor modeling with Ar, are shown in Figure 1 above this temperature. Oscillation regime was already observed and numerically predicted in previous studies with methane as fuel [58]; this is also an interesting topic of research but beyond the goals of the present work.

The kinetic mechanism is able to reproduce the experimental data, although the mole fraction of *n*-pentane is slightly overestimated at 625 K with Ar as the carrier gas. Below 800 K, the model predicts the same *n*-pentane conversion trend for He and Ar and a slightly lower conversion for CO_2. With respect to the CO formation, the model underestimates it with CO_2 as the bath gas when the temperature is above 1050 K.

Because the temperature is assumed to be uniform inside the reactor, the reactivity differences for different bath gases observed above 800 K might be ascribed rather to different third-body coefficients than to the different heat release rates due to thermal diffusion heat-transfer rates under the different bath gas environments. The branching mechanism represented by the reaction H_2O_2 (+M) = OH + OH (+M) is altered in virtue of the higher collisional efficiencies of CO_2 with respect to Ar and He. This is consistent with what was previously observed in ref [9]. At the highest temperatures, the reaction CO_2 + H = CO + OH explains why the CO amount is largest for the CO_2-diluted mixtures.

4.1.2. Oxidation of n-Pentane Doped with NOx

The results obtained between 500 and 900 K in the absence and in the presence of NO_x are presented in Figure 2.

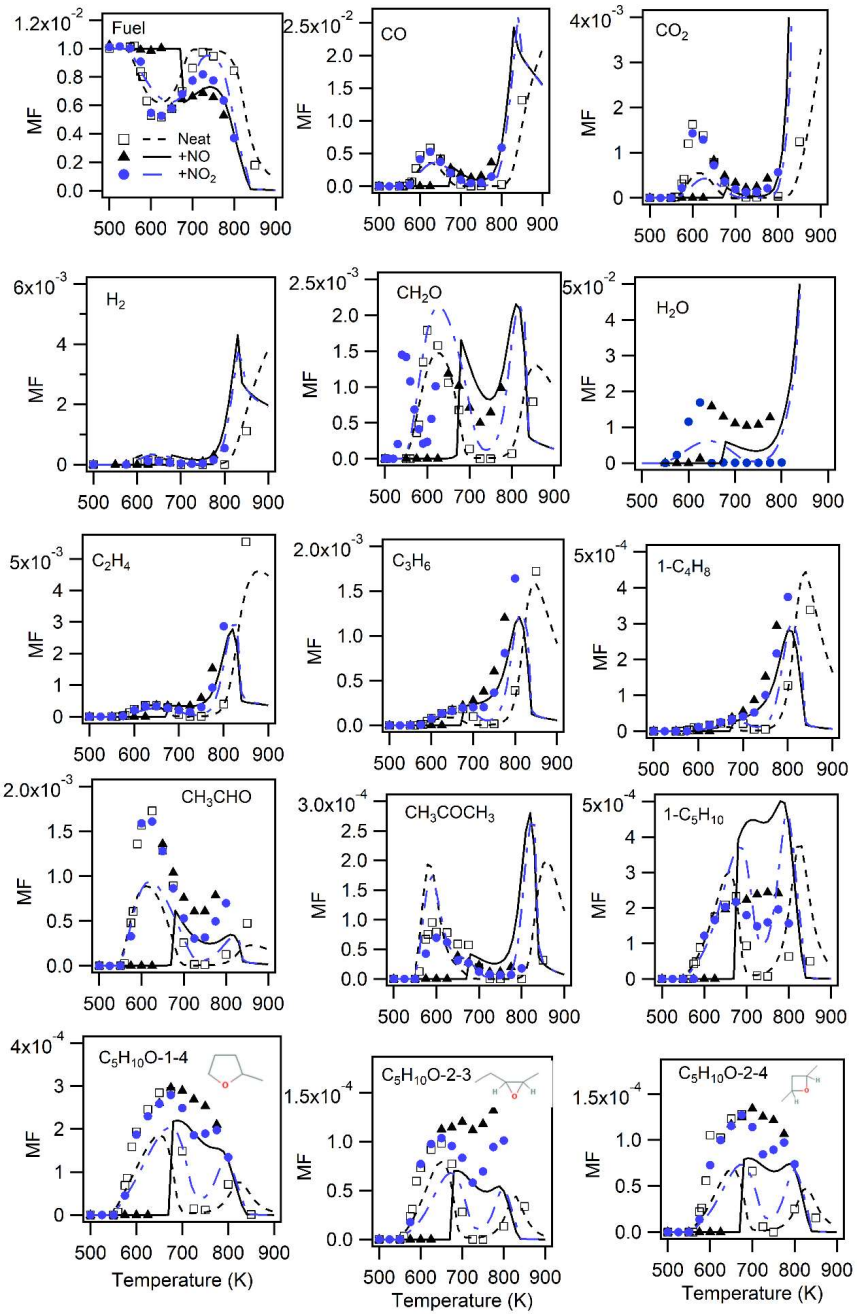

Figure 2. Influence of NO_x addition (with Ar as a bath gas) on the mole fractions of *n*-pentane and of its main oxidation products. Symbols represent experiments and lines represent simulations (empty squares and broken lines: no additive, black triangles and full lines: + NO, blue rounds and mixed lines: + NO_2).

In all the experiments with NOx addition, the carrier gas is Ar (exp. 5 and 6 in Table 2). Besides the temperature dependence of *n*-pentane mole fractions, the formation of some of the major reaction products is also displayed.

As it can be seen, the addition of 500 ppm NO (triangles) has a strong effect on the *n*-pentane reactivity. The onset temperature for *n*-pentane is shifted from 575 to 625 K by the addition of NO. This fact indicates that the presence of NO inhibits the reactivity of *n*-pentane in the NTC region. Above 700 K, the *n*-pentane conversion is larger in the presence of NO compared to the other two cases. On the other hand, the presence of 400 ppm NO_2 (circles) does not considerably modify the *n*-pentane mole fraction below 700 K. Above this temperature, the *n*-pentane conversion in the presence of NO_2 is in between that with added NO and that with neat *n*-pentane (squares).

With NO addition, the initial temperature for the formation of the main oxidation products, such as CO, H_2, C_2H_4, C_3H_6, 1-butene, 1-pentene, formaldehyde, acetaldehyde, acetone, and cyclic ethers ($C_5H_{10}O$-1-4 [2-methyltetrahydrofuran], $C_5H_{10}O$-2-4 [2,4-dimethyloxetane], and $C_5H_{10}O$-2-3 [methyl-ethyl-oxirane]), increases up to 650 K. For the products exhibiting an NTC area in neat mixtures, this behavior is significantly reduced in the presence of NO. NO_2 addition does not much alter the product formation below 700 K.

Overall, there is a good agreement between experimental data and model predictions, especially for light hydrocarbon species (C_2H_4, C_3H_6, and 1-C_4H_8). Moreover, the model can also predict quite well the profiles of H_2 and formaldehyde. More deviations are encountered for acetaldehyde and acetone. H_2O formation (not measured without additive) is also underestimated by the model, which was also observed in the previous methane and NO_x low-temperature oxidation work [44]. It might be ascribed to the uncertainty in cw-CRDS measurements because of its significant mole fraction. Regarding C_5 species, the model overestimates the mole fraction of 1-pentene and underestimates that of cyclic ethers. However, the difference in the shape of the temperature dependence profiles between neat mixture and with NO_x addition is well reproduced. As is shown by experiments, the strong mole fraction decreases, which is predicted between 700 and 800 K in neat mixture or with NO_2 addition, almost completely disappears with added NO.

In order to evaluate the effect of the amount of added NO on *n*-pentane oxidation, one more set of experiments in the presence of 1000 ppm NO was studied (exp. 4 in Table 2). As is shown in Figure 3, in the case of 1000 ppm of NO (blue circles), the onset temperature for *n*-pentane conversion is shifted from 625 K (500 ppm of NO) to 675 K. This implies that the retarding effect of NO on *n*-pentane oxidation is even stronger with the increase of the amount of added NO. Once the reaction is started, as temperature increases, the consumption of *n*-pentane is larger in the presence of 1000 ppm NO than that with only 500 ppm NO addition.

Figure 4 shows the temperature dependence of NO, NO_2, and HONO mole fractions in the presence of NO and NO_2. When its initial mole fraction is 500 ppm, NO starts to be consumed at 625 K; meanwhile, the mole fraction of NO_2 increases sharply to reach approximately 300 ppm. Above 650 K, NO is fully consumed, and the amount of NO_2 continues gradually increasing until 750 K. Concerning HONO, for which the quantification procedure under oxidation process was demonstrated elsewhere [45] its produced mole fraction is nearly 100 ppm at a temperature of 650 K. The HONO mole fraction also increases until the temperature is 725 K. After that, it decays as the temperature further increases.

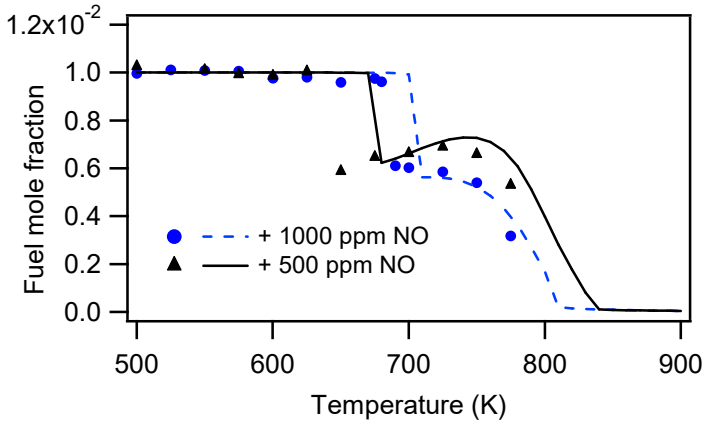

Figure 3. Mole fractions of *n*-pentane in the presence of NO (500 or 1000 ppm). Symbols are experiments, lines simulations.

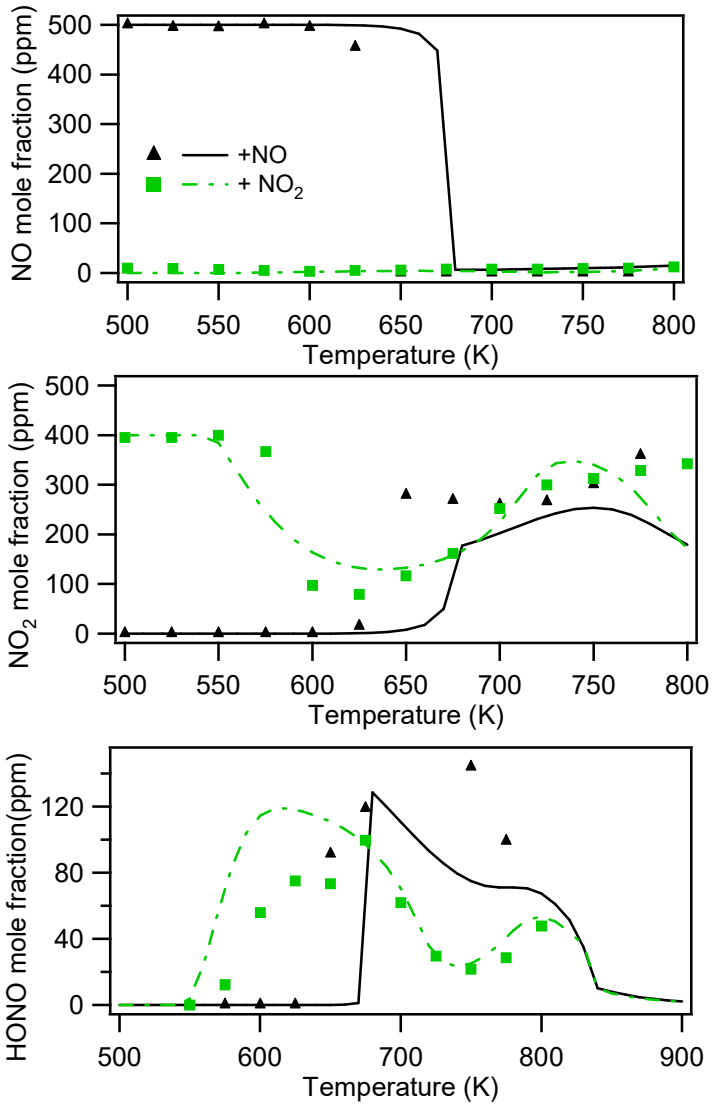

Figure 4. Temperature dependence of NO, NO_2, and HONO mole fractions in the presence of NO (500 ppm) or NO_2 (400 ppm). Symbols represents experiments and lines represent simulations.

When NO_2 (400 ppm) is added as a reactant, the onset temperature for its consumption is approximately 575 K, which is consistent with that of neat *n*-pentane as is shown in Figure 2. The NO_2 mole fraction drops to 90 ppm at a temperature of 625 K, and then it increases again with the increase of temperature. HONO mole faction gradually increases to 120 ppm when the temperature is 675 K. After that, the amount of HONO decreases to 70 ppm at 800 K. No NO formation is observed in the case of NO_2 addition, as it can be seen in the upper part of Figure 4.

With the aid of FTIR, a search for HCN (detection limit of 100 ppm [44]) and CH_3NO_2 (detection limit of 5 ppm [44]) species was attempted. However, there was no obvious signal of these two species on the spectra when compared to the standard ones at all the studied temperatures. The nitrogen mass balance significantly deteriorates in the temperature range from 600 to 700 K; this lack of nitrogen might be partly due to the detection limits of the current diagnostic instruments, but this is not fully understood.

The model captures satisfactorily the experimental trends for NO mole fractions. It slightly overestimates the amount of HONO when the temperature is below 650 K in the presence of NO, and in the case of NO_2 addition when the temperature is above 650 K. Regarding NO_2 addition, the model underestimates the produced mole fraction of NO_2 when the temperature is above 750 K. Note that the model predicts the formation of CH_3NO_2 and $C_2H_5NO_2$ in the presence of NO_x, especially in the 600–700 K temperature range, while none of these species was observed from an experimental point of view (the features present in the $C_2H_5NO_2$ FTIR spectrum of the NIST WebBook database [59] were not observed in our FTIR spectra). Simulations did not show notable amounts of HCN, but a maximum mole fraction of 40 ppm was predicted for CH_3NO_2 in the presence of NO and of 70 ppm in the presence of NO_2. Note that a notable formation of $C_2H_5NO_2$ was also predicted, with a maximum mole fraction of 130 ppm in the presence of NO and of 95 ppm in the presence of NO_2. More studies on the reactions of CH_3NO_2 and $C_2H_5NO_2$ would certainly be helpful to improve the model.

5. Discussion

Reaction rate and sensitivity analyses were performed to clarify the different reaction paths for the oxidation of *n*-pentane with and without NOx addition. Especially, the different low-temperature *n*-pentane oxidation behaviors with both NO and NO_2 addition and the HONO formation route were analyzed. A first characteristic temperature of 625 K, which is the typical of the low-temperature oxidation area, was selected to perform this analysis. The reaction paths for *n*-pentane consumption at this temperature are shown in Figure 5.

In the absence of NO_x, the *n*-pentane oxidation starts by H-abstractions by OH radicals. Depending on the H-abstraction site, three different pentyl radicals can be produced, although C_5H_{11}-2 is the predominant one. These pentyl radicals react with molecular oxygen to form $C_5H_{11}O_2$ radicals, which could readily isomerize to give $C_5H_{10}OOH$ radicals, even at this relatively low temperature. $C_5H_{10}OOH$ radicals then again add to O_2 and are a source of OH radicals and ketohydroperoxides, well-known branching agents. The decomposition of the main ketohydroperoxide obtained starting from C_5H_{11}-2 produces OH, CH_3CHO, and CH_3COCH_2. These last two species lead to the formation of CH_2O, acetone, and CO. The released OH radicals could then react again with the reactant, *n*-pentane. This sequence of reactions acts as a branching process, multiplying the number of radicals, therefore accelerating the whole system.

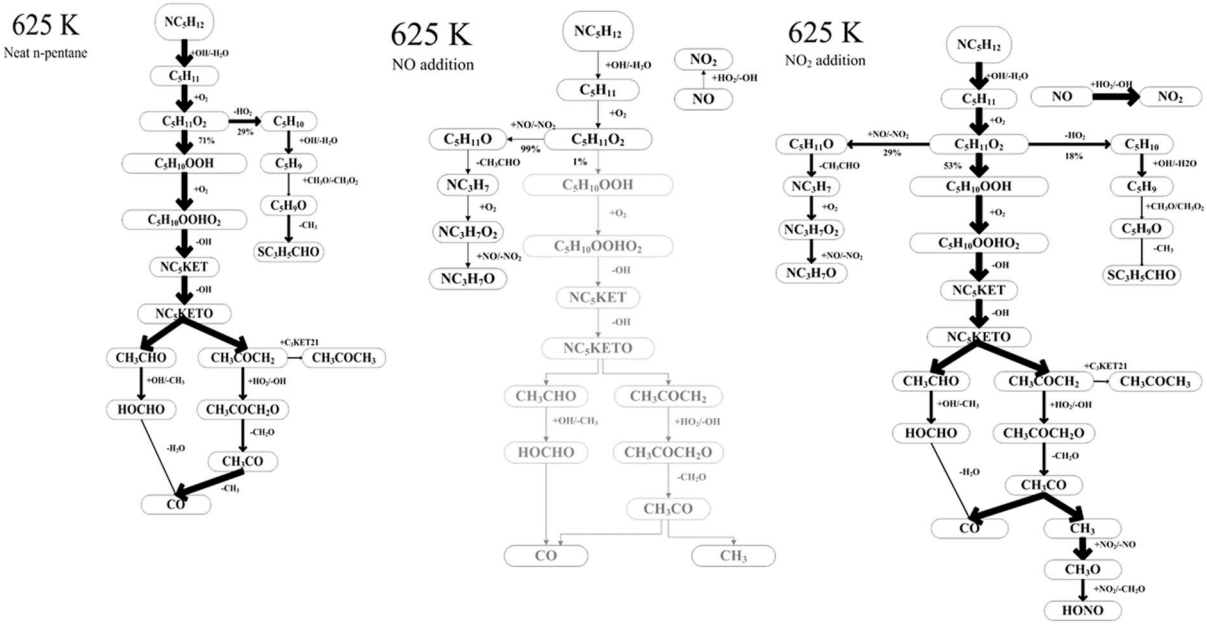

Figure 5. Reaction path diagram for *n*-pentane oxidation with or without NO_x addition at 625 K. The thickness of the arrow represents the flow rate of the corresponding reactions.

In the presence of NO, the route starting by the isomerization of $C_5H_{11}O_2$ to $C_5H_{10}OOH$ radicals, which is marked in gray in Figure 5, becomes almost negligible. Instead, with the aid of NO, $C_5H_{11}O_2$ converts to $C_5H_{11}O$ radicals. This explains why, under these conditions, *n*-pentane is barely consumed as is shown in Figure 2. $C_5H_{11}O$ radical decomposes to relatively unreactive species, CH_3CHO and NC_3H_7 radicals, compared to the highly reactive OH radicals derived from the presence of NO. Therefore, the route starting by the isomerization of $C_5H_{11}O_2$ to $C_5H_{10}OOH$ radicals, which is marked in gray in Figure 5, becomes almost negligible. It can be concluded that the self-sustained oxidation process with the help of OH radicals, formed in branching chains, is significantly disturbed by the addition of NO.

In the presence of NO_2, the major consumption route for NO_2 is $NO_2 + CH_3 = NO + CH_3O$, which has a minor direct effect on the *n*-pentane oxidation. Consequently, the *n*-pentane conversion displays a similar trend as that for the neat *n*-pentane as shown in Figure 2. Methyl radicals are produced via the ketohydroperoxide decomposition route. Meanwhile, the generated NO can somehow reduce the reactivity of the system as mentioned above. However, this effect is compensated by the fact that NO could convert back to NO_2 with the aid of HO_2, releasing OH radical ($NO + HO_2 = NO_2 + OH$), which can accelerate the *n*-pentane oxidation. Note that NO_2 can react with CH_3O radical to form HONO and CH_2O ($NO_2 + CH_3O = HONO + CH_2O$), explaining why, at 625 K, HONO is formed in the presence of NO_2 and not with NO, as is shown in Figure 4.

At an intermediate temperature of 725 K, the initial consumption route of neat *n*-pentane is still provided by the OH radical attack. However, once the $C_5H_{11}O_2$ radicals are generated, the main consumption route switches to decompose them directly to pentenes and HO_2 radicals. These last species are relatively stable and their formation competes with the branching route via ketohydroperoxides. Consequently, the fuel reactivity is dramatically hindered, and *n*-pentane mole fraction almost rebounds to the initial input value (see Figure 2). When added, NO can react

with the abundant HO_2 radicals, regenerating active OH radicals, which can accelerate the *n*-pentane oxidation. This explains why the *n*-pentane consumption remains significant from 675 to 725 K (see Figure 2). With respect to HONO, the formed NO_2 can further react with CH_3O and HO_2 radicals, along with CH_2O to form HONO, which can explain the high amount of HONO experimentally detected at 675 K. At the same temperature but in the presence of NO_2, the NO-HO_2 interaction cannot so easily induce additional OH radical formation and the temperature dependence of *n*-pentane mole fraction displays a similar trend compared to the neat *n*-pentane oxidation. In terms of HONO, its formation route is similar to that in the case of NO addition; however, the mole fraction of HONO is lower than that in the presence of NO; it might be ascribed to the lower initial mole fraction of NO_2 addition (400 ppm) compared to the NO addition (500 ppm).

The flow rate analysis displayed in Figure 6 was performed at a temperature of 775 K. The reaction paths, which are enclosed in the dash box, belong to the common *n*-pentane consumption routes with or without NOx addition. Note that, at this temperature, the importance of the channels associated with the *n*-pentane low-temperature oxidation is less important. The reactions of pentyl radicals by β-scission reactions (C_5H_{11}-2 leads to C_3H_6 and C_2H_5 radicals) and the formation of pentenes from peroxy radicals by HO_2-eliminations are favored and less OH radicals are produced via branching reactions.

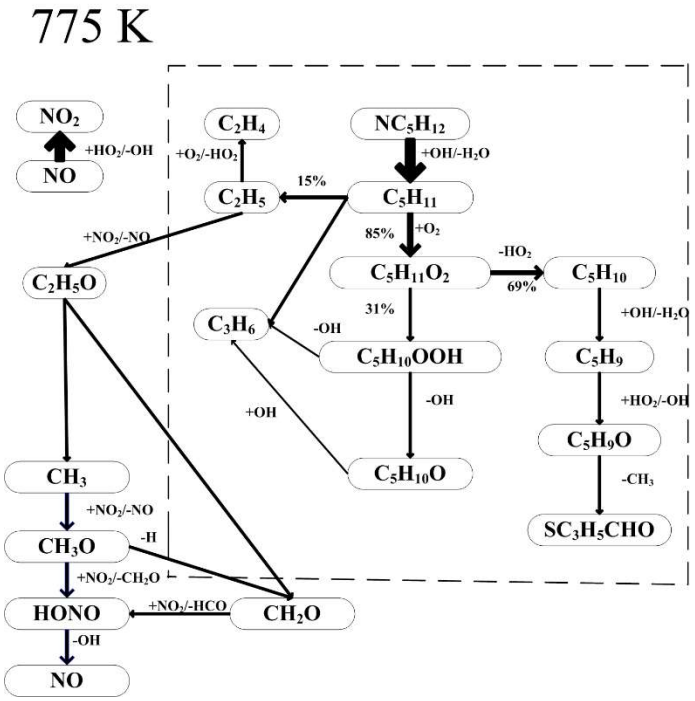

Figure 6. Reaction path diagram for *n*-pentane oxidation with NO addition at 775 K. The reaction paths, which are included in the dash box, belong to the common *n*-pentane consumption routes with or without NO_x addition. Only the decomposition pathways deriving from C_5H_{11}-2 are shown.

When added, NO can react with HO_2 radicals releasing OH radical and promoting *n*-pentane oxidation. C_2H_5 radical, produced from pentyl radical decomposition, could further react with O_2 to form C_2H_4 and HO_2, creating a second abundant source of this last radical. This is the reason why the *n*-pentane conversion in the presence of NO is faster than that in the case of neat

n-pentane oxidation. To a lower extent, a similar trend is observed when NO_2 is added. As NO is not present as a reactant, it is only produced by reactions of NO_2 with C_2H_5O or CH_3O radicals, which can react with HO_2 and be a source of OH radicals.

With respect to the HONO, in both NO and NO_2 cases, the main reaction routes are similar as mentioned at 725 K. However, the HONO dissociation reaction (HONO + M = OH + NO + M) is favored by the relative high temperature. The released OH radical could enhance the *n*-pentane oxidation as well.

Moreover, first-order sensitivity analyses were performed under the conditions of Figure 2 (Ar as bath gas) at 625 and 775 K. The sensitivity coefficients for *n*-pentane mole fractions are displayed in Figure 7. In this figure, reactions promoting *n*-pentane oxidation are indicated by negative sensitivity coefficients. Because at 625 K, in the presence of NO, no *n*-pentane consumption was observed in both experimental and model point of view, and no sensitivity analysis is presented at this temperature with added NO.

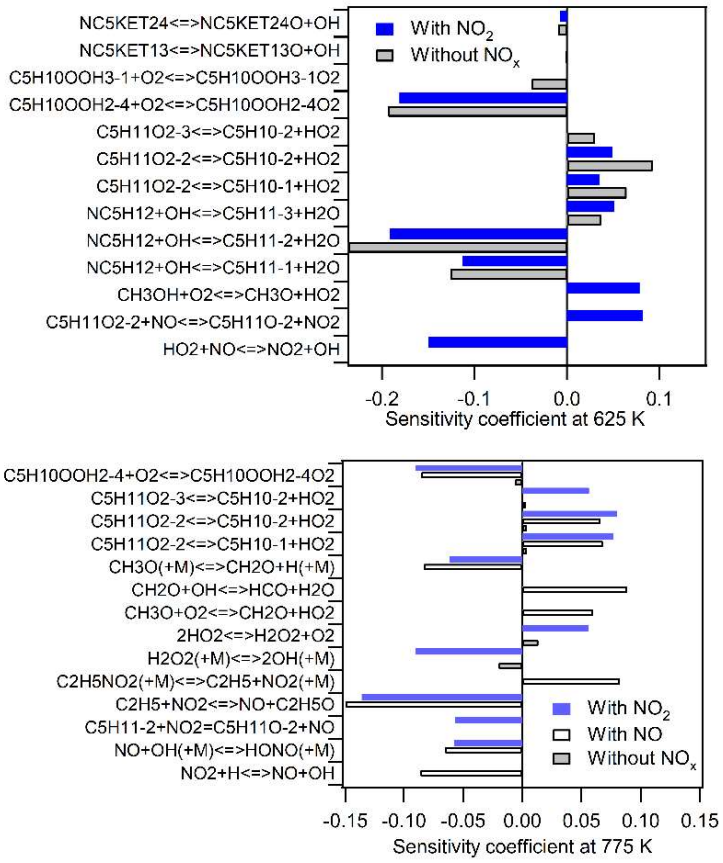

Figure 7. Sensitivity coefficient for *n*-pentane mole fraction at 625 and 775 K for neat *n*-pentane oxidation and in the presence of NO_2 or NO (only top 10 sensitive reactions are displayed).

For neat *n*-pentane, at 625 K, the reactions associated with OH radicals attacking *n*-pentane and leading to 1- and 2-pentyl radicals show the strongest negative sensitivity coefficients on *n*-pentane mole fraction, along with the addition to O_2 of the main hydroperoxypentyl radical obtained from 2-pentyl radicals, which is the main source of the OH radicals. Note that the H-abstractions leading to 3-pentyl radicals have some inhibiting effect. This is because the peroxy radicals obtained from 3-pentyl radicals isomerize less easily than those obtained from 1- and

2-pentyl radicals. The formation pathways of pentenes and HO_2 radicals inhibit the *n*-pentane oxidation, which is consistent with the reaction path analysis.

Figure 6 shows that, in the presence of NO_2, at 625 K, the reactions involving HO_2 radicals are particularly influential. In agreement with the flow rate analysis, the reaction of HO_2 radicals with NO to produce OH radicals has a strong promoting effect. The consumption by NO of the peroxy radicals deriving from 2-pentyl radicals to give alkoxy radicals has a significant inhibiting influence.

At 775 K, the NO_2–NO conversion reaction induced by C_2H_5 radical ($C_2H_5 + NO_2 = NO + C_2H_5O$) has a strong promoting effect on the *n*-pentane oxidation in the presence of both NO and NO_2. This effect is combined with that of the reactions releasing OH radicals or H atoms, such as $NO_2 + H = NO + OH$, $NO + OH + M = HONO + M$, $H_2O_2 + M = 2OH + M$, and $CH_3O + M = CH_2O + H + M$, as is shown by their large sensitivity coefficients.

Figure 8 presents the sensitivity analysis for HONO mole fraction at 625 and 775 K. Positive coefficients indicate reactions favoring HONO formation. Because at 625 K, in the presence of NO, no HONO formation was reported in both experiments and modeling, no HONO sensitivity analysis is displayed at this temperature with added NO.

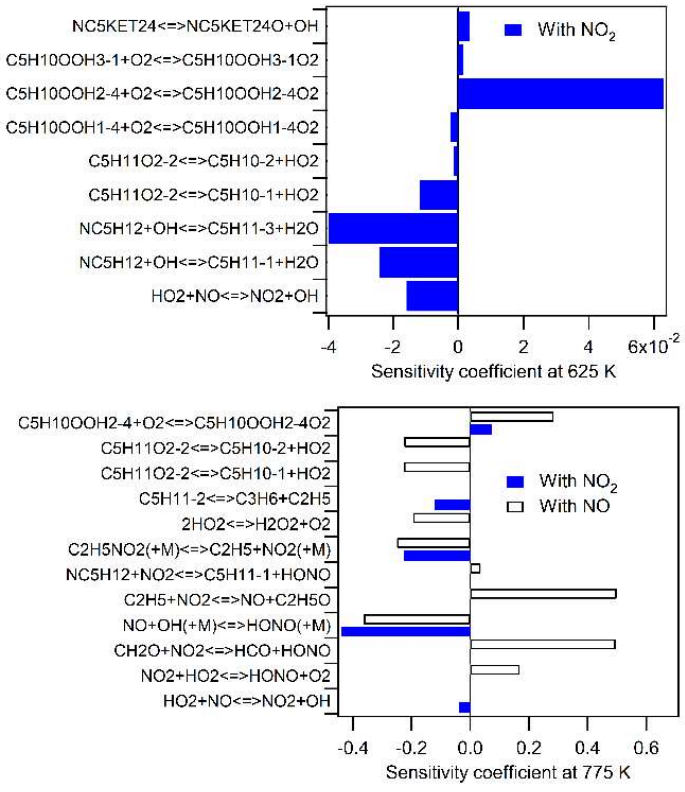

Figure 8. Sensitivity coefficient for HONO mole fraction at 625 and 775 K for neat *n*-pentane oxidation and in the presence of NO_2 or NO (only top 10 sensitive reactions are displayed).

At 625 K, in the presence of NO_2, the most significant HONO reaction promoting formation is the addition to O_2 of the main hydroperoxypentyl radical obtained from 2-pentyl radicals. This is because this reaction favors the overall reactivity, but more especially because it leads to the formation of the ketohydroperoxides, the decomposition of which is the source of CH_3O radicals.

The reaction of these last radicals with NO_2 is responsible for more than 80% of HONO formation at this temperature. The H-abstractions from *n*-pentane competing with the formation of 2-pentyl radicals have a negative influence on HONO formation.

At 775 K, both with NO and NO_2 addition, again the addition to O_2 of the main hydroperoxypentyl radical obtained from 2-pentyl radicals shows a notable sensitivity toward HONO formation. The reactions associated with C_2H_5O, a precursor of CH_3O radicals, CH_2O, and HO_2 radicals play an important role in promoting HONO formation. The HONO decomposition has the strongest depleting influence on the nitrogenated species.

6. Conclusions

This work presents an investigation of the oxidation of *n*-pentane in a JSR from both experimental and modeling points of view. Experiments were carried out at 107 kPa and temperatures between 500 and 1100 K with a fixed residence time of 2.0 s under stoichiometric conditions. The effects of different bath gases (He, Ar, and CO_2) as well as NO_2 and NO in Ar on fuel reactivity were studied. Note that HONO quantification was performed with the help of cw-CRDS. In general, there is a good agreement between experimental results and model predictions.

The obtained experimental results are almost identical with the different kinds of bath gases in low-temperature oxidation. Above 800 K, the fuel reactivity is affected by the bath gas in the order CO_2 > Ar > He. With CO_2 as a carrier gas, CO formation is larger than those with He and Ar as carrier gases. Moreover, the addition of NO_2 also produces comparable results, except for the largest conversion of *n*-pentane when the temperature is above 700 K. On the contrary, in the presence of NO, we observed a significant delay of the initial temperature for the start of *n*-pentane oxidation. The onset temperatures of HONO formation in the presence of NO_2 and NO are 575 and 650 K, respectively.

Kinetic analysis showed that the different behaviors of NO and NO_2 addition on *n*-pentane oxidation are related to their roles in the NO_x submechanism. As for NO, the $C_5H_{11}O_2 + NO = C_5H_{11}O + NO_2$ reaction alters the main route of $C_5H_{11}O_2$ consumption, leading to chain-branching at low temperature, and therefore strongly hinders the reactivity of the system. With respect to NO_2, the $NO_2 + CH_3 = NO + CH_3O$ reaction is responsible for the NO_2 consumption and has a less directly relevant effect on low-temperature *n*-pentane oxidation. This can account for the diverse *n*-pentane oxidation behavior with NO and NO_2 addition. The reactions associated with NO_2 and CH_iO (i = 2, 3) are mainly responsible for the HONO formation, regardless of NO or NO_2 addition, the reverse of OH + NO + M = HONO + M reaction is the major source of HONO depletion.

An extension of this work at higher pressures and for various fuels (e.g., *n*-heptane) or biofuels would certainly be of interest.

Supporting Information

Complete mechanism including species and reactions
Thermodynamic data for the involved species
Experimental data including N-atom balance
Experimental data from the literature

References

1. Kalghatgi, G. T. Proc. Combust. Inst. 2015, 35, 101– 115, DOI: 10.1016/j.proci.2014.10.002
2. Liu, F.; Guo, H.; Smallwood, G. J.; Gülder, Ö. L. Combust. Flame 2001, 125, 778– 787, DOI: 10.1016/s0010-2180(00)00241-8
3. Giménez-López, J.; Millera, A.; Bilbao, R.; Alzueta, M. U. Combust. Flame 2010, 157, 267– 276, DOI: 10.1016/j.combustflame.2009.07.016
4. Anderlohr, J. M.; Pires da Cruz, A.; Bounaceur, R.; Battin-Leclerc, F. Combust. Sci. Technol. 2010, 182, 39–59, DOI: 10.1080/00102200903190844
5. Abián, M.; Giménez-López, J.; Bilbao, R.; Alzueta, M. U. Proc. Combust. Inst. 2011, 33, 317– 323, DOI: 10.1016/j.proci.2010.05.078
6. Schönborn, A.; Sayad, P.; Konnov, A. A.; Klingmann, J. Combust. Flame 2013, 160, 1033– 1043, DOI: 10.1016/j.combustflame.2013.01.018
7. Sabia, P.; Lubrano Lavadera, M.; Giudicianni, P.; Sorrentino, G.; Ragucci, R.; de Joannon, M. Combust. Flame 2015, 162, 533– 543, DOI: 10.1016/j.combustflame.2014.08.009
8. Sabia, P.; Lubrano Lavadera, M.; Sorrentino, G.; Giudicianni, P.; Ragucci, R.; de Joannon, M. Flow, Turbul. Combust. 2016, 96, 433– 448, DOI: 10.1007/s10494-015-9667-4
9. Lubrano Lavadera, M.; Sabia, P.; Sorrentino, G.; Ragucci, R.; de Joannon, M. Fuel 2016, 184, 876– 888, DOI: 10.1016/j.fuel.2016.06.046
10. Di, H.; He, X.; Zhang, P.; Wang, Z.; Wooldridge, M. S.; Law, C. K.; Wang, C.; Shuai, S.; Wang, J. Combust. Flame 2014, 161, 2531– 2538, DOI: 10.1016/j.combustflame.2014.04.014
11. Zhang, X.; Ye, W.; Shi, J. C.; Wu, X. J.; Zhang, R. T.; Luo, S. N. Energy Fuels 2017, 31, 12780– 12790, DOI: 10.1021/acs.energyfuels.7b01632
12. Mathieu, O.; Pemelton, J. M.; Bourque, G.; Petersen, E. L. Combust. Flame 2015, 162, 3053– 3070, DOI: 10.1016/j.combustflame.2015.03.024
13. Sivaramakrishnan, R.; Brezinsky, K.; Dayma, G.; Dagaut, P. Phys. Chem. Chem. Phys. 2007, 9, 4230– 4244, DOI: 10.1039/b703379f
14. Herzler, J.; Naumann, C. Combust. Sci. Technol. 2012, 184, 1635– 1650, DOI: 10.1080/00102202.2012.690617
15. Gokulakrishnan, P.; Fuller, C. C.; Klassen, M. S.; Joklik, R. G.; Kochar, Y. N.; Vaden, S. N.; Lieuwen, T. C.; Seitzman, J. M. Combust. Flame 2014, 161, 2038– 2053, DOI: 10.1016/j.combustflame.2014.01.024
16. Bromly, J. H.; Barnes, F. J.; Muris, S.; You, X.; Haynes, B. S. Combust. Sci. Technol. 1996, 115, 259– 296, DOI: 10.1080/00102209608935532
17. Alzueta, M. U.; Glarborg, P.; Dam-Johansen, K. Combust. Flame 1997, 109, 25– 36, DOI: 10.1016/s0010-2180(96)00146-0
18. Glarborg, P.; Alzueta, M. U.; Dam-Johansen, K.; Miller, J. A. Combust. Flame 1998, 115, 1– 27, DOI: 10.1016/s0010-2180(97)00359-3
19. Bendtsen, A. B.; Glarborg, P.; Dam-Johansen, K. Combust. Sci. Technol. 2000, 151, 31– 71, DOI: 10.1080/00102200008924214
20. Dagaut, P.; Luche, J.; Cathonnet, M. Proc. Combust. Inst. 2000, 28, 2459– 2465, DOI: 10.1016/s0082-0784(00)80660-8
21. Dagaut, P.; Nicolle, A. Combust. Flame 2005, 140, 161– 171, DOI: 10.1016/j.combustflame.2004.11.003
22. Rasmussen, C. L.; Rasmussen, A. E.; Glarborg, P. Combust. Flame 2008, 154, 529– 545, DOI: 10.1016/j.combustflame.2008.01.012
23. Mendiara, T.; Glarborg, P. Energy Fuels 2009, 23, 3565– 3572, DOI: 10.1021/ef9001956
24. Chan, Y. L.; Barnes, F. J.; Bromly, J. H.; Konnov, A. A.; Zhang, D. K. Proc. Combust. Inst. 2011, 33, 441– 447, DOI: 10.1016/j.proci.2010.05.029
25. Giménez-López, J.; Aranda, V.; Millera, A.; Bilbao, R.; Alzueta, M. U. Fuel Process. Technol. 2011, 92, 582–589, DOI: 10.1016/j.fuproc.2010.11.014
26. Chan, Y. L.; Bromly, J. H.; Konnov, A. A.; Zhang, D. K. Combust. Sci. Technol. 2012, 184, 114– 132, DOI: 10.1080/00102202.2011.622320

27. Zhang, J.; Burklé-Vitzthum, V.; Marquaire, P. M. Combust. Sci. Technol. 2015, 187, 1139– 1156, DOI: 10.1080/00102202.2015.1019617
28. Chakir, A.; Belumam, M.; Boettner, J. C.; Cathonnet, M. Combust. Sci. Technol. 1991, 77, 239– 260, DOI: 10.1080/00102209108951730
29. Simon, V.; Simon, Y.; Scacchi, G.; Baronnet, F. Can. J. Chem. 1997, 75, 575– 584, DOI: 10.1139/v97-068
30. Bugler, J.; Rodriguez, A.; Herbinet, O.; Battin-Leclerc, F.; Togbé, C.; Dayma, G.; Dagaut, P.; Curran, H. J. Proc. Combust. Inst. 2017, 36, 441– 448, DOI: 10.1016/j.proci.2016.05.048
31. Rodriguez, A.; Herbinet, O.; Wang, Z.; Qi, F.; Fittschen, C.; Westmoreland, P. R.; Battin-Leclerc, F. Proc. Combust. Inst. 2017, 36, 333– 342, DOI: 10.1016/j.proci.2016.05.044
32. Marks, B.; Mathieu, O.; Archuleta, R.; Petersen, E.; Metcalfe, W.; Curran, H.; Bourque, G. In 51st AIAA Aerospace Sciences Meeting Including the New Horizons Forum and Aerospace Exposition; American Institute of Aeronautics and Astronautics, 2013.
33. Bugler, J.; Marks, B.; Mathieu, O.; Archuleta, R.; Camou, A.; Grégoire, C.; Heufer, K. A.; Petersen, E. L.; Curran, H. J. Combust. Flame 2016, 163, 138– 156, DOI: 10.1016/j.combustflame.2015.09.014
34. Zhukov, V.; Sechenov, V.; Starikovskii, A. Combust. Flame 2005, 140, 196– 203, DOI: 10.1016/j.combustflame.2004.11.008
35. Jin, H.; Pieper, J.; Hemken, C.; Bräuer, E.; Ruwe, L.; Kohse-Höinghaus, K. Combust. Flame 2018, 193, 36– 53, DOI: 10.1016/j.combustflame.2018.03.003
36. Prabhu, S.; Bhat, R. K.; Miller, D. L.; Cernansky, N. P. Combust. Flame 1996, 104, 377– 390, DOI: 10.1016/0010-2180(95)00134-4
37. Glaude, P. A.; Marinov, N.; Koshiishi, Y.; Matsunaga, N.; Hori, M. Energy Fuels 2005, 19, 1839– 1849, DOI: 10.1021/ef050047b
38. Zhao, H.; Wu, L.; Patrick, C.; Zhang, Z.; Rezgui, Y.; Yang, X.; Wysocki, G.; Ju, Y. Combust. Flame 2018, 197, 78– 87, DOI: 10.1016/j.combustflame.2018.07.014
39. Zhao, H.; Dana, A. G.; Zhang, Z.; Green, W. H.; Ju, Y. Energy 2018, 165, 727– 738, DOI: 10.1016/j.energy.2018.10.013
40. Perner, D.; Platt, U. Geophys. Res. Lett. 1979, 6, 917– 920, DOI: 10.1029/gl006i012p00917
41. Karlsson, R. S.; LjungstrÖm, E. B. Environ. Sci. Technol. 1996, 30, 2008– 2013, DOI: 10.1021/es950801f
42. Jain, C.; Morajkar, P.; Schoemaecker, C.; Viskolcz, B.; Fittschen, C. J. Phys. Chem. A 2011, 115, 10720– 10728, DOI: 10.1021/jp203001y
43. Chai, J.; Goldsmith, C. F. Proc. Combust. Inst. 2017, 36, 617– 626, DOI: 10.1016/j.proci.2016.06.133
44. Song, Y.; Marrodán, L.; Vin, N.; Herbinet, O.; Assaf, E.; Fittschen, C.; Stagni, A.; Faravelli, T.; Alzueta, M. U.; Battin-Leclerc, F. Proc. Combust. Inst. 2018, 37, 667– 675, DOI: 10.1016/j.proci.2018.06.115
45. Marrodán, L.; Song, Y.; Herbinet, O.; Alzueta, M. U.; Fittschen, C.; Ju, Y.; Battin-Leclerc, F. Chem. Phys. Lett. 2019, 719, 22– 26, , in press DOI: 10.1016/j.cplett.2019.01.038
46. Herbinet, O.; Battin-Leclerc, F. Int. J. Chem. Kinet. 2014, 46, 619– 639, DOI: 10.1002/kin.20871
47. Bahrini, C.; Herbinet, O.; Glaude, P.-A.; Schoemaecker, C.; Fittschen, C.; Battin-Leclerc, F. Chem. Phys. Lett. 2012, 534, 1– 7, DOI: 10.1016/j.cplett.2012.03.012
48. Anderlohr, J.; Bounaceur, R.; Piresdacruz, A.; Battin-Leclerc, F. Combust. Flame 2009, 156, 505– 521, DOI: 10.1016/j.combustflame.2008.09.009
49. Glarborg, P.; Bendtsen, A. B.; Miller, J. A. Int. J. Chem. Kinet. 1999, 31, 591– 602, DOI: 10.1002/(sici)1097-4601(1999)31:9<591::aid-kin1>3.0.co;2-e
50. Atkinson, R.; Baulch, D. L.; Cox, R. A.; Hampson, R. F.; Kerr, J. A.; Troe, J. J. Phys. Chem. Ref. Data 1992, 21, 1125– 1568, DOI: 10.1063/1.555918
51. Tsang, W.; Herron, J. T. J. Phys. Chem. Ref. Data 1991, 20, 609– 663, DOI: 10.1063/1.555890
52. Glaude, P. A.; Conraud, V.; Fournet, R.; Battin-Leclerc, F.; Côme, G. M.; Scacchi, G.; Dagaut, P.; Cathonnet, M. Energy Fuels 2002, 16, 1186– 1195, DOI: 10.1021/ef020025e
53. Chan, W.-T.; Heck, S. M.; Pritchard, H. O. Phys. Chem. Chem. Phys. 2001, 3, 56– 62, DOI: 10.1039/b006088g
54. Choi, Y. M.; Lin, M. C. Int. J. Chem. Kinet. 2005, 37, 261– 274, DOI: 10.1002/kin.20079
55. Atkinson, R.; Baulch, D. L.; Cox, R. A.; Crowley, J. N.; Hampson, R. F.; Hynes, R. G.; Jenkin, M. E.; Rossi, M. J.; Troe, J. Atmos. Chem. Phys. 2004, 4, 1461– 1738, DOI: 10.5194/acp-4-1461-2004

56. Burkholder, J. B.; Mellouki, A.; Talukdar, R.; Ravishankara, A. R. Int. J. Chem. Kinet. 1992, 24, 711– 725, DOI: 10.1002/kin.550240805
57. CHEMKIN-PRO 15151; Reaction Design: San Diego, 2013.
58. Lubrano Lavadera, M.; Song, Y.; Sabia, P.; Herbinet, O.; Pelucchi, M.; Stagni, A.; Faravelli, T.; Battin-Leclerc, F.; de Joannon, M. Energy Fuels 2018, 32, 10088– 10099, DOI: 10.1021/acs.energyfuels.8b00967
59. NIST Chemistry WebBook, NIST Standard Reference Database Number 69; Linstrom, P. J., Mallard, W. G., Eds.; National Institute of Standards and Technology: Gaithersburg MD, 20899, 2017.